

Mass accretion to young stars triggered by flaring activity in circumstellar disks

Salvatore Orlando¹ *, Fabio Reale^{2,1}, Giovanni Peres^{2,1}, Andrea Mignone³

¹*INAF - Osservatorio Astronomico di Palermo, Piazza del Parlamento 1, 90134, Palermo, Italy*

²*Dip. di Fisica, Università degli Studi di Palermo, Piazza del Parlamento 1, 90134, Palermo, Italy*

³*Dip. di Fisica Generale, Università degli Studi di Torino, via Pietro Giuria 1, 10125, Torino, Italy*

Accepted. Received

ABSTRACT

Young low-mass stars are characterized by ejection of collimated outflows and by circumstellar disks which they interact with through accretion of mass. The accretion builds up the star to its final mass and is also believed to power the mass outflows, which may in turn remove the excess angular momentum from the star-disk system. However, although the process of mass accretion is a critical aspect of star formation, some of its mechanisms are still to be fully understood. A point not considered to date and relevant for the accretion process is the evidence of very energetic and frequent flaring events in these stars. Flares may easily perturb the stability of the disks, thus influencing the transport of mass and angular momentum. Here we report on three-dimensional magnetohydrodynamic modeling of the evolution of a flare with an idealized non-equilibrium initial condition occurring near the disk around a rotating magnetized star. The model takes into account the stellar magnetic field, the gravitational force, the viscosity of the disk, the magnetic-field-oriented thermal conduction (including the effects of heat flux saturation), the radiative losses from optically thin plasma, and the coronal heating. We show that, during its first stage of evolution, the flare gives rise to a hot magnetic loop linking the disk to the star. The disk is strongly perturbed by the flare: disk material evaporates under the effect of the thermal conduction and an overpressure wave propagates through the disk. When the overpressure reaches the opposite side of the disk, a funnel flow starts to develop there, accreting substantial disk material onto the young star from the side of the disk opposite to the flare.

Key words: accretion, accretion disks – MHD – stars: circumstellar matter – stars: flare – stars: pre-main-sequence – X-rays: stars.

1 INTRODUCTION

Classical T Tauri Stars (CTTSs) are young low-mass stars actively accreting mass from a surrounding disk (Hartmann 1998; Bouvier & Appenzeller 2007). On the basis of the largely accepted magnetospheric accretion scenario (Koenigl 1991), the accretion process from the disk is regulated by the stellar magnetic field which is strong enough to disrupt the inner part of the disk at a distance of a few stellar radii (the truncation radius) where the magnetic pressure is approximately equal to the total gas pressure. The field guides the circumstellar material along its flux tubes toward the central protostar, around free-fall velocity, terminating in a shock at the photosphere. This scenario is supported by much obser-

vational evidence, among others, the photospheric magnetic field of a few kG that has been detected in a number of CTTSs by exploiting the Zeeman effect (Johns-Krull et al. 1999).

One of the fundamental issues in the magnetospheric accretion scenario is the mechanism of inward transport of matter and outward transport of angular momentum needed to explain the final mass and angular momentum of mature stars. The turbulence in the disk has been proposed to be the main responsible of the required outward angular momentum transport, thus controlling the mass accretion on the central star (Shakura & Sunyaev 1973). Nowadays, there is a large consensus in the literature that the turbulence is mainly driven by the magnetorotational instability (MRI; Balbus & Hawley 1991, 1998). MRI operates in regions where the ionization is sufficient to couple the gas to the

* E-mail: orlando@astropa.inaf.it

magnetic field and leads to the transfer of angular momentum along the magnetic field lines connecting gas located in different orbits (Hawley et al. 1995; Brandenburg et al. 1995; Armitage 1998; Hawley 2000; Hirose et al. 2006). Despite the significant theoretical progress achieved in this field, the details of this transport mechanism have yet to be fully understood, and it is not clear if MRI alone is able to account for the mass accretion and for the removal of excess angular momentum (King et al. 2007; Fromang & Papaloizou 2007; Bodo et al. 2008). Given the complexity of this mechanism and our poor knowledge of its details, the efficiency of angular momentum transport within the disk is often modeled in the literature by including a viscosity in the disk modulated via an analogue of the Shakura-Sunyaev α -parameter (Shakura & Sunyaev 1973) which can be expressed in terms of the fluctuating velocity and magnetic field (Romanova et al. 2002, 2003; Kulkarni & Romanova 2008).

On the other hand, observations in the X-ray band have shown that pre-main-sequence stars are strong sources with X-ray luminosity 3-4 orders of magnitude greater than that of the present-day Sun (Getman et al. 2005; Audard et al. 2007). The source of this X-ray radiation is a plasma at 1 – 100 MK in the stellar outer atmospheres (coronae), heated by magnetic activity analogous to the solar one but much stronger (Feigelson & Montmerle 1999). X-ray flares are violent manifestations of this magnetic activity and are triggered by an impulsive energy input from coronal magnetic field. X-ray observations in the last decades have shown that flares in CTTSs have amplitudes larger than solar analogues and occur much more frequently (Favata et al. 2005; Getman et al. 2005; Audard et al. 2007; Aarnio et al. 2010). Examples of these flares are those collected by the Chandra satellite in the Orion star-formation region (COUP enterprise; Favata et al. 2005). The analysis of these flares revealed that they have peak temperatures often in excess of 100 MK, are long-lasting, and are confined in very long magnetic structures – extending for several stellar radii – which may connect the star’s photosphere with the accretion disk (structures that could be of the same kind as those which channel the plasma in the magnetospheric accretion).

At the present time, it is unclear where these flares occur. The differential rotation of the disk together with the interaction of the disk with the magnetosphere may cause magnetic reconnection close to the disk’s surface, triggering large-scale flares there. In this case, the flares may perturb the stability of the circumstellar disk causing, in particular, a strong local overpressure. The pressure gradient force might be able to push disk’s matter out of the equatorial plane into funnel streams, thus providing a mechanism to drive mass accretion that differs from that, commonly invoked in the literature, based on the disk viscosity which determines the accumulation of disk matter and the increase of gas pressure close to the truncation radius (Romanova et al. 2002). Bright flares close to circumstellar disks may therefore have important implications for a number of issues such as the transfer of angular momentum and mass between the star and the disk, the powering of outflows, and the ionization of circumstellar disks thus influencing also the efficiency of MRI (see also Aarnio et al. 2010).

In this paper, we investigate the effects of a flare on the stability of the circumstellar disk with a three-dimensional

(3D) magnetohydrodynamic (MHD) simulation. We model the evolution of the star-disk plasma heated by a strong energy release (with intensity comparable to that of flares typically observed in young stars), close to a thick disk surrounding a rotating magnetized CTTS. The model takes into account all key physical processes, including the gravitational force, the viscosity of the disk, the magnetic-field-oriented thermal conduction, the radiative losses from optically thin plasma, and the coronal heating. The wealth of nonlinear physical processes governing the star-disk system and the evolution of the flare made this a challenging task. In Sect. 2 we describe the MHD model and the numerical setup; in Sect. 3 we describe the results; in Sect. 4 we discuss the implications of our results and draw our conclusions.

2 PROBLEM DESCRIPTION AND NUMERICAL SETUP

Our model describes a large flare in a rotating magnetized star surrounded by a thick quasi-Keplerian disk. The flare occurs close to the inner portion of the disk, within the corotation radius (i.e. where a Keplerian orbit around the star has the same angular velocity as the star’s surface), where accretion streams are expected to originate (Romanova et al. 2002; Bessolaz et al. 2008). The magnetic field of the star is aligned dipole-like, with intensity $B \approx 1$ kG at the stellar surface according to observations (Johns-Krull et al. 1999). The fluid is assumed to be fully ionized with a ratio of specific heats $\gamma = 5/3$.

2.1 MHD equations

The system is described by the time-dependent MHD equations in a 3D spherical coordinate system (R, θ, ϕ) , extended with gravitational force, viscosity of the disk, thermal conduction (including the effects of heat flux saturation), coronal heating (via a phenomenological term), and radiative losses from optically thin plasma. To our knowledge, this is the first numerical time-dependent global simulation of the star-disk system that takes into account simultaneously all key physical ingredients necessary to describe accurately the effects of a flare on the structure of the circumstellar disk. The time-dependent MHD equations written in non-dimensional conservative form are:

$$\frac{\partial \rho}{\partial t} + \nabla \cdot (\rho \vec{u}) = 0, \quad (1)$$

$$\frac{\partial \rho \vec{u}}{\partial t} + \nabla \cdot (\rho \vec{u} \vec{u} - \vec{B} \vec{B} + \vec{I} P_t - \vec{\tau}) = \rho \vec{g}, \quad (2)$$

$$\frac{\partial \rho E}{\partial t} + \nabla \cdot [\vec{u}(\rho E + P_t) - \vec{B}(\vec{u} \cdot \vec{B}) - \vec{u} \cdot \vec{\tau}] = \rho \vec{u} \cdot \vec{g} - \nabla \cdot \vec{F}_c - n_e n_H \Lambda(T) + Q(R, \theta, \phi, t), \quad (3)$$

$$\frac{\partial \vec{B}}{\partial t} + \nabla \cdot (\vec{u} \vec{B} - \vec{B} \vec{u}) = 0, \quad (4)$$

where

$$P_t = P + \frac{\vec{B} \cdot \vec{B}}{2}, \quad E = \epsilon + \frac{\vec{u} \cdot \vec{u}}{2} + \frac{\vec{B} \cdot \vec{B}}{2\rho},$$

are the total pressure, and the total gas energy per unit mass (internal energy, ϵ , kinetic energy, and magnetic energy) respectively, t is the time, $\rho = \mu m_H n_H$ is the mass density, $\mu = 1.28$ is the mean atomic mass (assuming metal abundances of 0.5 of the solar values; Anders & Grevesse 1989), m_H is the mass of the hydrogen atom, n_H is the hydrogen number density, \vec{u} is the gas velocity, $\vec{\tau}$ is the viscous stress tensor, $\vec{g} = \nabla\Phi_g$ is the gravity acceleration vector, $\Phi_g = -GM_*/R$ is the gravitational potential of a central star of mass M_* , G is the gravitational constant, R is the distance from the gravitating center, T is the temperature, \vec{B} is the magnetic field, \vec{F}_c is the thermal conductive flux, $\Lambda(T)$ represents the optically thin radiative losses per unit emission measure derived with the PINTofALE spectral code (Kashyap & Drake 2000) and with the APED V1.3 atomic line database (Smith et al. 2001), assuming the same metal abundances as before (as deduced from X-ray observations of CTTSS; Telleschi et al. 2007), and $Q(R, \theta, \phi, t)$ is a function of space and time describing the phenomenological heating rate (see Sect. 2.3). We use the ideal gas law, $P = (\gamma - 1)\rho\epsilon$.

The viscosity is assumed to be negligible in the extended stellar corona and effective only in the circumstellar disk. In order to make the transition between the disk and the corona, we track the original disk material by using a tracer that is passively advected in the same manner as the density. We define C_{disk} the mass fraction of the disk inside the computational cell. The disk material is initialized with $C_{\text{disk}} = 1$, while $C_{\text{disk}} = 0$ in the extended corona. Then the viscosity works only in zones consisting of the original disk material by more than 99% or, in other words, where $C_{\text{disk}} > 0.99$. The viscous stress tensor is defined as

$$\vec{\tau} = \eta_\nu \left[(\nabla\vec{u}) + (\nabla\vec{u})^T - \frac{2}{3}(\nabla \cdot \vec{u})\vec{I} \right], \quad (5)$$

where $\eta_\nu = \nu_\nu \rho$ is the dynamic viscosity, and ν_ν is the kinematic viscosity. Several studies suggest that turbulent diffusion of magnetic field in the disk is determined by the same processes that determine turbulent viscosity, leading to angular momentum transport in the disk (Bisnovatyi-Kogan & Lovelace 2001). Thus, we assume that turbulent magnetic diffusivity is of the same order of magnitude as turbulent viscosity like in the Shakura-Sunyaev model (Shakura & Sunyaev 1973). The kinematic viscosity is expressed as $\nu_\nu = \alpha c_s^2 / \Omega_K$, where c_s is the isothermal sound speed, Ω_K is the Keplerian angular velocity at a given location, and $\alpha < 1$ is a dimensionless parameter regulating the efficiency of angular momentum transport within the disk, which can be expressed in terms of the fluctuating velocity and magnetic field. The parameter α varies in the range 0.01 – 0.6 in the Shakura-Sunyaev accretion model (Balbus 2003). In our simulation, we assume $\alpha = 0.02$.

The thermal conduction is highly anisotropic due to the presence of the stellar magnetic field, the conductivity being highly reduced in the direction transverse to the field (Spitzer 1962). The thermal flux therefore is locally split into two components, along and across the magnetic field lines, $\vec{F}_c = F_{\parallel} \vec{i} + F_{\perp} \vec{j}$. The thermal conduction formulation also accounts for heat flux saturation. In fact, during early phases of flares, rapid transients, fast dynamics and steep thermal gradients are known to develop (Reale & Orlando 2008). Under these circumstances the conditions required for classical ‘‘Spitzer’’ heat conduction may break down to

the extent that the plasma thermal conduction becomes flux limited (Brown et al. 1979). The two components of thermal flux are therefore written as (Orlando et al. 2008, 2010)

$$F_{\parallel} = \left(\frac{1}{[q_{\text{spi}}]_{\parallel}} + \frac{1}{[q_{\text{sat}}]_{\parallel}} \right)^{-1}, \quad (6)$$

$$F_{\perp} = \left(\frac{1}{[q_{\text{spi}}]_{\perp}} + \frac{1}{[q_{\text{sat}}]_{\perp}} \right)^{-1},$$

to allow for a smooth transition between the classical and saturated conduction regime, where $[q_{\text{spi}}]_{\parallel}$ and $[q_{\text{spi}}]_{\perp}$ represent the classical conductive flux along and across the magnetic field lines (Spitzer 1962)

$$[q_{\text{spi}}]_{\parallel} = -\kappa_{\parallel} [\nabla T]_{\parallel} \approx -9.2 \times 10^{-7} T^{5/2} [\nabla T]_{\parallel} \quad (7)$$

$$[q_{\text{spi}}]_{\perp} = -\kappa_{\perp} [\nabla T]_{\perp} \approx -3.3 \times 10^{-16} \frac{n_H^2}{T^{1/2} B^2} [\nabla T]_{\perp},$$

where $[\nabla T]_{\parallel}$ and $[\nabla T]_{\perp}$ are the thermal gradients along and across the magnetic field, and κ_{\parallel} and κ_{\perp} (in units of $\text{erg s}^{-1} \text{K}^{-1} \text{cm}^{-1}$) are the thermal conduction coefficients along and across the magnetic field, respectively. The saturated flux along and across the magnetic field lines, $[q_{\text{sat}}]_{\parallel}$ and $[q_{\text{sat}}]_{\perp}$, are (Cowie & McKee 1977)

$$[q_{\text{sat}}]_{\parallel} = -\text{sign}([\nabla T]_{\parallel}) 5\varphi \rho c_s^3, \quad (8)$$

$$[q_{\text{sat}}]_{\perp} = -\text{sign}([\nabla T]_{\perp}) 5\varphi \rho c_s^3,$$

where φ is a number of the order of unity; we set $\varphi = 1$ according to the values suggested for stellar coronae (Giuliani 1984; Borkowski et al. 1989; Fadeyev et al. 2002).

The calculations were performed using PLUTO (Mignone et al. 2007), a modular, Godunov-type code for astrophysical plasmas. The code provides a multiphysics, multialgorithm modular environment particularly oriented toward the treatment of astrophysical flows in the presence of discontinuities as in the case treated here. The code was designed to make efficient use of massive parallel computers using the message-passing interface (MPI) library for interprocessor communications. The MHD equations are solved using the MHD module available in PLUTO, configured to compute intercell fluxes with the Harten-Lax-Van Leer approximate Riemann solver, while second order in time is achieved using a Runge-Kutta scheme. A Van Leer limiter for the primitive variables is used during the heating release (at the very beginning of the simulation for $t < 300$ s) and a monotonized central difference limiter at other times. The evolution of the magnetic field is carried out adopting the constrained transport approach (Balsara & Spicer 1999) that maintains the solenoidal condition ($\nabla \cdot \vec{B} = 0$) at machine accuracy. We adopted the ‘‘magnetic field-splitting’’ technique (Tanaka 1994; Powell et al. 1999; Zanni & Ferreira 2009) by splitting the total magnetic field into a contribution coming from the background stellar magnetic field and a deviation from this initial field. Then only the latter component is computed numerically. This approach is particularly useful when dealing with low- β plasma as it is the case in proximity of the stellar surface (Zanni & Ferreira 2009). PLUTO includes optically thin radiative losses in a fractional step formalism (Mignone et al. 2007), which preserves the 2^{nd} time accuracy, as the ad-

vection and source steps are at least of the 2^{nd} order accurate; the radiative losses Λ values are computed at the temperature of interest using a table lookup/interpolation method. The thermal conduction is treated separately from advection terms through operator splitting. In particular we adopted the super-time-stepping technique (Alexiades et al. 1996) which has been proved to be very effective to speed up explicit time-stepping schemes for parabolic problems. This approach is crucial when high values of plasma temperature are reached (as during flares), explicit scheme being subject to a rather restrictive stability condition (i.e. $\Delta t < (\Delta x)^2/(2\eta)$, where η is the maximum diffusion coefficient), as the thermal conduction timescale τ_{cond} is shorter than the dynamical one τ_{dyn} (e.g. Hujerirat & Camenzind 2000; Hujerirat 2005; Orlando et al. 2005, 2008); in particular, during the early phases of the flare evolution, we find $\tau_{\text{cond}}/\tau_{\text{dyn}} \approx 10^{-2}$. The viscosity is solved with an explicit scheme, using a second-order finite difference approximation for the dissipative fluxes.

2.2 Initial and boundary conditions

A star of mass $M_* = 0.8M_\odot$ and radius $R_* = 2R_\odot$ is located at the origin of the 3D spherical coordinate system (R, θ, ϕ) , with the rotation axis coincident with the normal to the disk midplane. The rotation period of the star is assumed to be 9.2 days. The initial unperturbed stellar atmosphere is approximately in equilibrium and consists of three components: the stellar magnetosphere, the extended stellar corona, and the quasi-Keplerian disk.

The pre-flare magnetosphere is assumed to be force-free, with dipole topology and magnetic moment μ_B aligned with the rotation axis of the star. Thus the two field components in spherical coordinates are

$$B_R = \frac{2\mu_B \cos \theta}{R^3}, \quad B_\theta = \frac{\mu_B \sin \theta}{R^3}. \quad (9)$$

The magnetic moment is chosen in order to have a magnetic field strength of the order of 1 kG at the stellar surface according to observations (Johns-Krull et al. 1999).

The initial corona and disk are set in order to satisfy mechanical equilibrium involving centrifugal, gravitational, and pressure gradient forces. In particular, we adopted the initial conditions introduced by Romanova et al. (2002) (where the reader is referred to for more details) and describing the star-disk system in quiescent configuration. These conditions assume that initially the plasma is barotropic and that the disk and the corona are both isothermal with temperatures T_d and T_c , respectively. With these assumptions, the thermal pressure at any point of the spatial domain is given by

$$P = \begin{cases} P_0 \exp\left[\mathcal{F} \frac{\mu m_H}{2T_c}\right] & P \leq P_0, \\ P_0 \exp\left[\mathcal{F} \frac{\mu m_H}{2T_d}\right] & P \geq P_0, \end{cases} \quad (10)$$

where $P_0 = 2\rho_c k_B T_c / (\mu m_H)$ is the initial pressure at the boundary between the disk and the corona, ρ_c is the mass density of the corona close to the disk truncation radius R_d , k_B is the Boltzmann constant, \mathcal{F} is the function

$$\mathcal{F} = (k-1) \frac{GM_*}{R_d} - (\Phi_g + \Phi_c), \quad (11)$$

k is a constant of the order of 1 that takes into account

that the disk is slightly non-Keplerian (we set $k = 1.01$ as in Romanova et al. 2002), Φ_c is the centrifugal potential written as

$$\Phi_c = \begin{cases} k \frac{GM_*}{R_d} \left[1 + \frac{R_d^2 - r^2}{2R_d^2}\right] & r \leq R_d, \\ k \frac{GM_*}{r} & r \geq R_d, \end{cases} \quad (12)$$

and $r = R \sin \theta$ is the cylindrical radius. The mass density depends on the pressure given in Eq. 10 at any point of the spatial domain

$$\rho(P) = \begin{cases} \frac{\mu m_H P}{2T_c} & P < P_0, \\ \frac{\mu m_H P}{2T_d} & P > P_0. \end{cases} \quad (13)$$

The angular velocity of the plasma is given by

$$\omega = \begin{cases} \left(k \frac{GM_*}{R_d^3}\right)^{1/2} & r \leq R_d, \\ \left(k \frac{GM_*}{r^3}\right)^{1/2} & r \geq R_d. \end{cases} \quad (14)$$

In our simulation, we assume the isothermal disk to be cold ($T_d = 8 \times 10^3$ K), dense (n_d ranges between 5×10^{11} and 4×10^{12} cm $^{-3}$), and to rotate with angular velocity close to the Keplerian value Ω_K . The rotation axis of the disk (coincident with the rotation axis of the star) is aligned with the magnetic moment μ_B . The disk is initially truncated by the stellar magnetosphere at the radius R_d where the total gas pressure of the disk equals the magnetic pressure, $p + \rho u^2 = B^2/8\pi$; for the parameters adopted here, $R_d = 2.86 R_*$. In our simulation, the corotation radius $R_{\text{co}} = (GM_*/\Omega_*^2)^{1/3} = 9.2 R_*$, where Ω_* is the stellar angular velocity. The corona is initially isothermal with $T_c = 4$ MK and at low density¹ with n_c ranging between $\approx 10^8$ and 10^9 cm $^{-3}$. As shown in Eq. 14, we allow the corona to be initially rotating with angular velocity equal to the Keplerian rotation rate of the disk in order to have approximately equilibrium conditions and reduce the effects of transients caused by the initial differential rotation between the disk and the corona (Romanova et al. 2002; Zanni & Ferreira 2009).

Figure 1 shows the initial condition together with the numerical grid adopted in our simulation. The computational domain extends between $R_{\text{min}} = R_*$ (i.e. the inner boundary coincides with the stellar surface) and $R_{\text{max}} = 14 R_*$ in the radial direction, and encompasses an angular sector going from $\theta_{\text{min}} = 5^\circ$ to $\theta_{\text{max}} = 175^\circ$ in the angular coordinate θ , and from $\phi_{\text{min}} = 0^\circ$ to $\phi_{\text{max}} = 360^\circ$ in the angular coordinate ϕ . The inner and outer boundaries in θ do not coincide with the rotation axis of the star-disk system to avoid extremely small $\delta\phi$ values, vastly increasing the computational cost. On the other hand, all the evolution relevant for this study never involve portions of the domain close to the star-disk rotation axis.

The radial coordinate R has been discretized on a logarithmic grid with the mesh size increasing with R (see Fig. 1), giving a higher spatial resolution closer to the star as it is appropriate for simulations of accretion flows to a star with a dipole field (Romanova et al. 2002). The radial

¹ Note however that the density of the outer corona is not important for the flare evolution.

grid is made of $N_R = 80$ points with a maximum resolution of $\Delta R = 4.8 \times 10^9$ cm close to the star and a minimum resolution of $\Delta R = 6.4 \times 10^{10}$ cm close to the outer boundary. The angular coordinate θ has been discretized uniformly with $N_\theta = 90$ points, giving a resolution of $\Delta\theta = 2^\circ$. The angular coordinate ϕ is nonuniform with the highest resolution in an angular sector of 180° placed where the flaring loop and the stream evolve (see bottom panel in Fig. 1). The ϕ -grid is made of $N_\phi = 110$ points with a maximum resolution of $\Delta\phi = 2^\circ$ and a minimum resolution of 9° . The numerical grid is not static but tracks the hot loop and the stream as the calculation progresses, in such a way that the loop and the stream evolve in the portion of the domain with the highest spatial resolution (namely that with $\Delta\phi = 2^\circ$).

The boundary conditions at the stellar surface R_{\min} amount to assuming that the infalling material passes through the surface of the star as done by Romanova et al. (2002) (outflows boundary condition; see also Romanova et al. 2003; Kulkarni & Romanova 2008), thus ignoring the dynamics of the plasma after it impacts on the star. Zero-gradient boundary conditions are assumed at the outer boundary of the coordinate R (R_{\max}) and at the boundaries of the angular coordinate θ (θ_{\min} and θ_{\max}). Finally, periodic boundary conditions are assumed for angular coordinate ϕ (ϕ_{\min} and ϕ_{\max}).

2.3 Coronal heating and flare

The phenomenological heating is prescribed as a component, describing the stationary coronal heating, plus a transient component, triggering a flare. The former component works at temperature $T \leq 4$ MK and is chosen to balance exactly the local radiative losses, leading to a quasi-stationary extended corona during the whole simulation. The transient component describes the injection of a heating pulse at the surface of the accretion disk. The flare could be driven by a stressed field configuration resulting from the twisting of magnetic field lines induced by the differential rotation of the inner rim of the disk and the stellar photosphere (Shu et al. 1997). The heat pulse has a 3D Gaussian spatial distribution located at the disk border at a distance of $5 R_*$ (namely well below the corotation radius $R_{\text{co}} = 9.2 R_*$) with width $\sigma = 2 \times 10^{10}$ cm. Its intensity per unit volume is $H_0 = 32$ ergs $\text{cm}^{-3} \text{s}^{-1}$. The pulse starts at the beginning of the simulation ($t = 0$) and is switched off completely after 300 s. The flare parameters are analogous to those adopted in a one-dimensional (1D) hydrodynamic model that reproduces the evolution of a large flare observed in an Orion young star from COUP (Favata et al. 2005). The total energy released during our simulated flare is $E_{\text{fl}} = 10^{36}$ ergs, namely the same order of magnitude of the energy involved in the brightest X-ray flares observed in COUP (Favata et al. 2005; Wolk et al. 2005).

3 RESULTS

3.1 Evolution of the flare and X-ray emission

We followed the evolution of the star-disk system for ≈ 2 days, focusing on its effects on the disk structure. Figure 2 shows the distributions of density and temperature in (R, z)

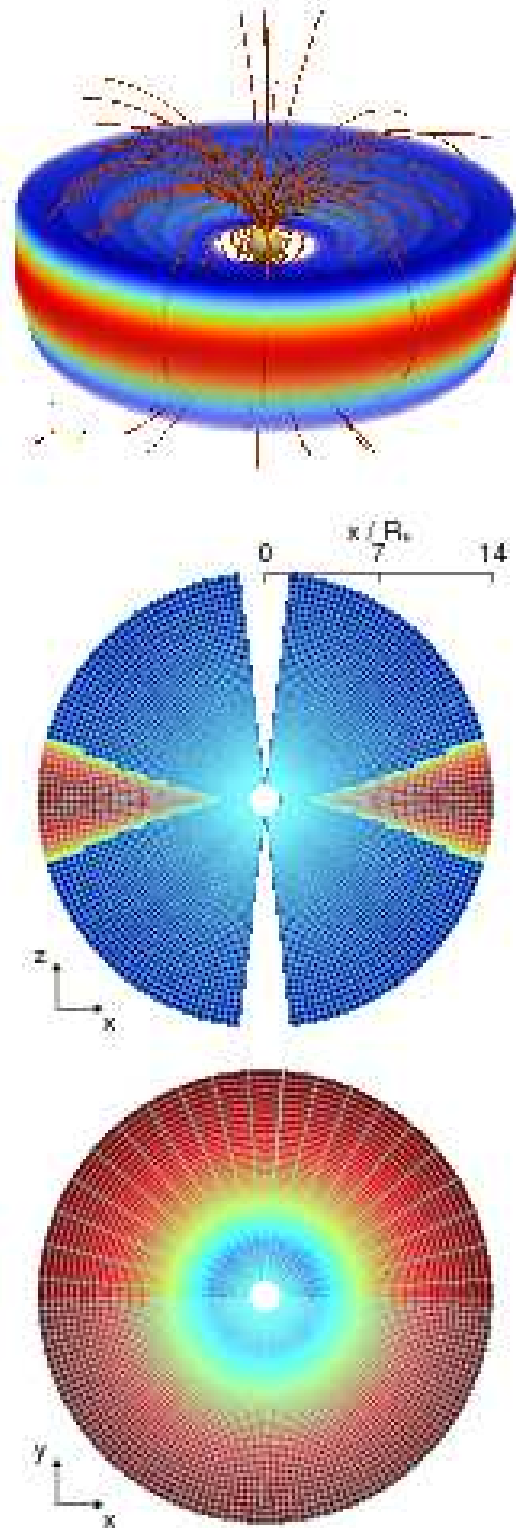


Figure 1. Initial conditions and computational domain. *Upper panel:* volume rendering of the mass density, in log scale, at the beginning of the simulation ($t = 0$). The selected magnetic field lines marked in red describe the initial dipolar magnetic field. The yellow sphere at the center of the spatial domain represents the central protostar. *Middle panel:* slice in the (x, z) plane of the mass density distribution with overplotted the computational grid. *Bottom panel:* as in the middle panel for the slice in the equatorial plane (x, y) .

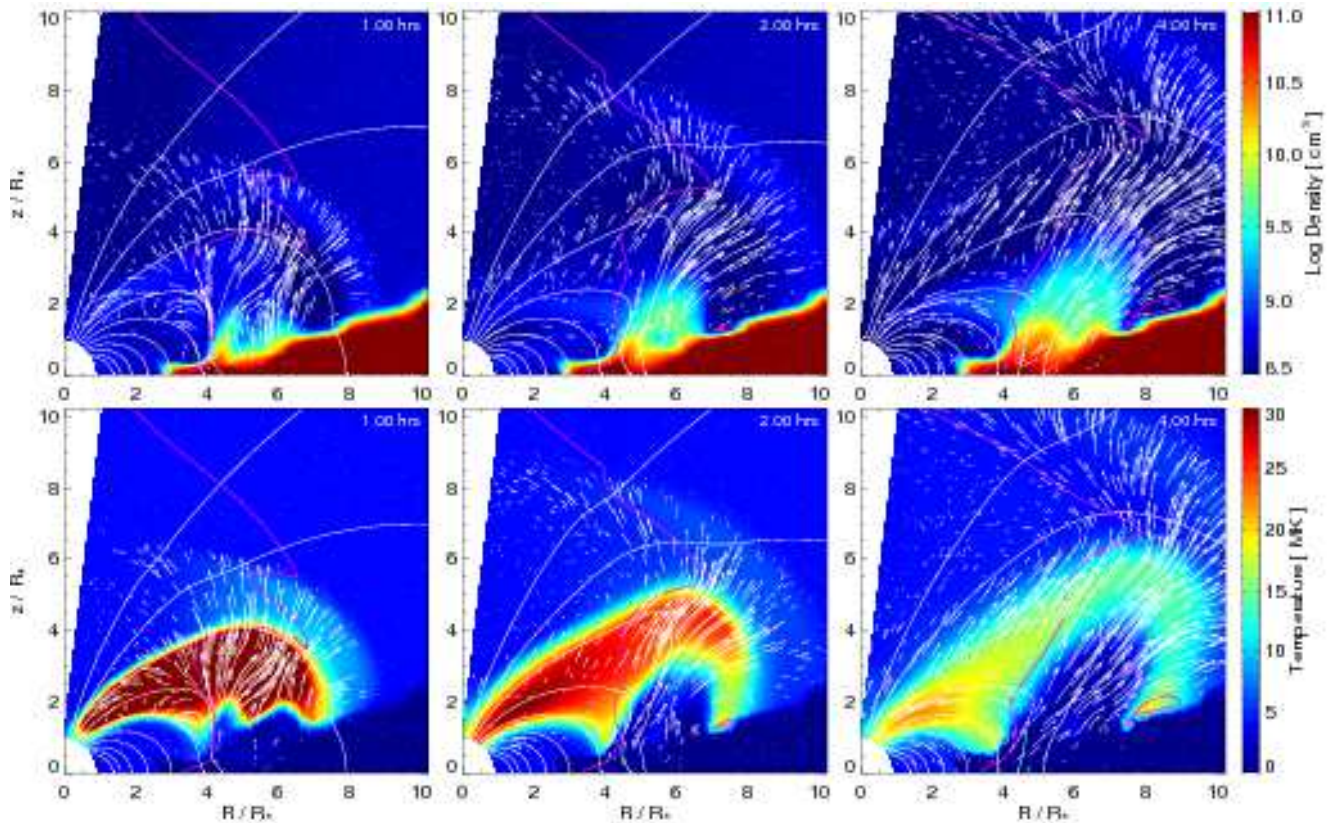


Figure 2. Close view of the flaring loop during its early evolution. The figure shows slices in the (R, z) plane passing through the middle of the flaring loop, reporting the distributions of density (upper panels) and temperature (lower panels). The slices encompass an angular sector going from the rotation axis to the disk midplane. The white lines represent sampled poloidal magnetic field lines. The arrows represent the poloidal flow velocities. The magenta line delimits the region with plasma $\beta < 1$ (on the left of each panel).

slices passing through the middle of the heating pulse during its evolution. During this impulsive phase, the local magnetic field is perturbed by the flare and an MHD shock wave develops in the magnetosphere above the disk and propagates radially away from the central protostar in regions where $\beta > 1$. At the same time, the sudden heat deposition determines a local increase of temperature (up to a maximum of 800 MK) and pressure (above 6000 dyn cm^{-2}). The dense disk material is heated and expands in the magnetosphere with a strong evaporation front at speeds above 4000 km s^{-1} . The fast thermal front propagates toward the star along the magnetic field lines and reaches the stellar surface on a timescale of ≈ 1 hour (left panels in Fig. 2). At this point, a hot magnetic tube (loop) of length $L \approx 10^{12} \text{ cm}$ (i.e. comparable to loop lengths inferred from COUP observations; Favata et al. 2005) is formed, linking the inner part of the disk to the star’s photosphere. The loop is illustrated in the left panels of Fig. 3 showing a cutaway view of the star-disk system at $t = 1.2$ hours (upper panel; the flaring loop is marked in red), and a schematic view of the system during the evolution of the flaring loop (lower panel). Due to the efficient thermal conduction and radiation, the plasma begins to cool immediately after the heat pulse is over, and the maximum temperature rapidly decreases to $\sim 50 \text{ MK}$ in ≈ 1 hour. The disk evaporation is fed by thermal conduction from the outer hot plasma, even after the end of the heat pulse.

Figure 2 also shows that the overheating of the disk surface at the loop footpoint makes a significant amount of material expand and be ejected in the magnetosphere. A small fraction of this evaporated disk material streams along the loop accelerated toward the star by its gravity, fills the whole tube in ≈ 10 hours, and the density keeps increasing throughout the loop up to values ranging between 10^9 and 10^{10} cm^{-3} at its apex. On the other hand, most of the evaporated disk material is not efficiently confined by the magnetic field and channeled into the hot loop but is rather ejected away from the central star in the outer stellar corona, carrying away mass and angular momentum (see Fig. 2). Due to the high values of β there, the magnetic field lines are dragged away. The outflowing plasma is supersonic and its speed is of the order of the local Alfvén speed $u_A \approx 300 \text{ km s}^{-1}$. We note that our results on the dynamics of the outflowing plasma are similar to those found with an MHD model proposed by Hayashi et al. (1996) to describe hard X-ray flares in protostars observed by the ASCA satellite.

From the model results, we synthesized the X-ray emission originating from the flare, applying a methodology analogous to that described in the literature in the context of the study of novae and supernova remnants (Orlando et al. 2006, 2009). In particular, we first calculate the emission measure in the j -th domain cell as $\text{em}_j = n_{\text{H}j}^2 V_j$ (where $n_{\text{H}j}^2$ is the hydrogen number density in the cell, V_j is the cell volume, and we assume fully ionized plasma). From

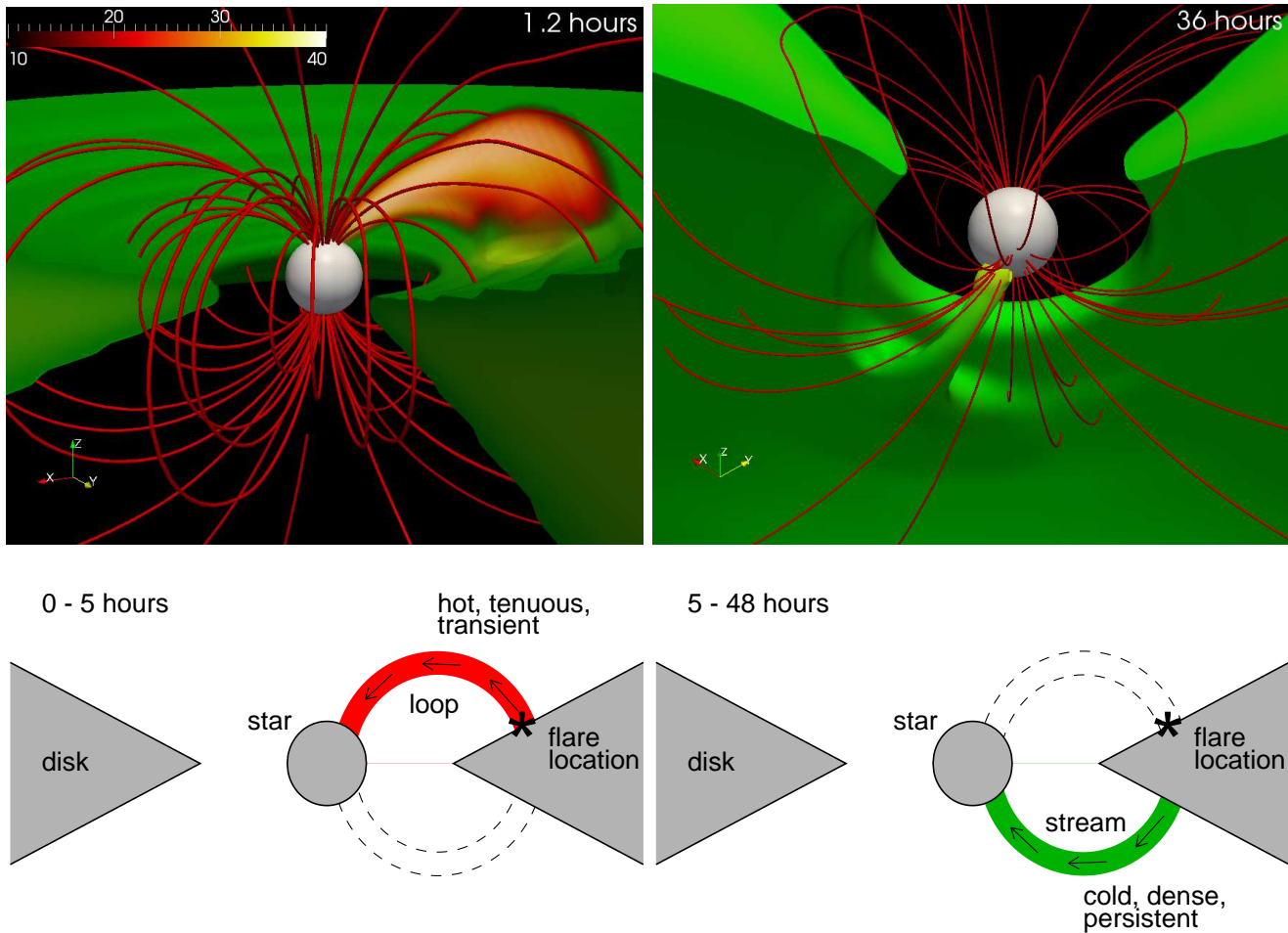


Figure 3. Evolution of the bright flare and accretion stream. The upper panels show cutaway views of the star-disk system showing the mass density of the disk (green) at $t = 1.2$ hours (on the left) and, from the opposite side, at $t = 36$ hours (on the right) since the injection of the heat pulse. The upper left panel also overplots the three-dimensional volume rendering of the plasma temperature (in MK; see color table in the upper left corner of the panel), showing the flaring loop (in red) linking the inner part of the disk with the star. The upper right panel shows the accretion stream triggered by the flare in the side of the disk opposite to the flaring loop. Selected magnetic field lines are overplotted in red. Lower panels show schematic views of the system during the evolution of the flaring loop (on the left) and in the subsequent period, during the evolution of the stream (on the right).

the values of emission measure and temperature in the cell, we synthesize the corresponding X-ray spectrum, using the PINToFALE spectral code (Kashyap & Drake 2000) with the APED V1.3 atomic line database, and assuming the same metal abundances of the simulation, namely 0.5 of the solar values, as deduced from X-ray observations of CTTSs (Telleschi et al. 2007). We integrate the X-ray spectra from the cells in the whole spatial domain and, then, derive the X-ray luminosity by integrating the spectrum in the $[0.6 - 12]$ keV band.

Figure 4 shows the evolution of the maximum temperature and emission measure of the flaring loop, and its X-ray lightcurve. The peak temperature of the flare is reached very soon at $t \approx 100$ s, the emission measure peaks later at $t \approx 1000$ s. The X-ray luminosity evolves as the emission measure, reaching a peak value of $L_X \approx 6.5 \times 10^{32}$ ergs s^{-1} at $t \approx 500$ s, namely after the end of the heat pulse. Then the luminosity (and the emission measure) decreases by more than two orders of magnitude until $t \approx 3 \times 10^3$ s, is steady

till $t \approx 2 \times 10^4$ s, and decreases again afterward. The peak X-ray luminosity of the simulated flare is consistent with the values derived for the brightest X-ray flares observed in COUP (see Table 1 in Favata et al. 2005) which range between 10^{32} ergs s^{-1} (source COUP 752) and 8×10^{32} ergs s^{-1} (source COUP 1568). On the other hand, it turns out that 3/4 of the COUP flares have a peak X-ray luminosity approximately one order of magnitude lower than that simulated here although the total energy released during the simulated flare (namely $E_{\text{fl}} = 10^{36}$ ergs, see Sect. 2.3) is comparable with the median total energy of the flare inferred from the COUP observations (Wolk et al. 2005). This may be due to the fact that the simulated flare lasts for a time interval significantly shorter than those typical of stellar flares and is only partially confined by the magnetic field (see discussion below).

The evolution of our simulated flare has significant differences with respect to the evolution of flares simulated with 1D models (Reale et al. 1988). In fact, at variance with

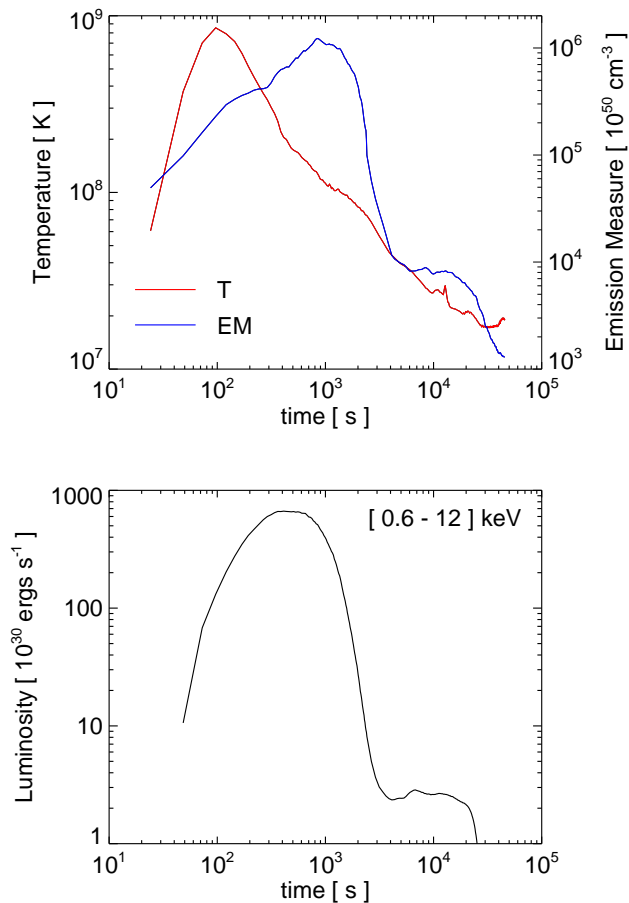


Figure 4. *Upper panel:* evolution of maximum temperature (red line) and emission measure (blue line) of the flaring loop. *Lower panel:* X-ray lightcurve of the flare in the [0.6 – 12] keV band.

1D models where the flare is assumed to be fully confined by the magnetic field, in our simulation the flare is only partially confined by the magnetic field at the loop footpoint anchored at the disk surface. There, a substantial amount of the evaporated disk material escapes in the outer stellar magnetosphere and does not fill the post-flare loop. We conclude therefore that our results could be intermediate between those found with models of fully confined flares (Reale et al. 1988) and those of models of unconfined flares (Reale et al. 2002) which show that the flare evolution is much faster than that observed in the confined case. On the other hand, for the purposes of this work (namely the study of the perturbation of the disk by a bright flare), we have used a simplified and idealized configuration of the initial stellar magnetic field (namely a magnetic dipole), whilst many observations indicate that the stellar atmospheres are permeated by magnetic fields with a high degree of complexity (e.g. Gregory et al. 2010 and references therein). In particular, the magnetic field in proximity of a heat release (due to magnetic reconnection) near the disk is expected to be more complex than that modeled here. In the presence of complex magnetic field configurations, the magnetic structure hosting the flaring plasma is expected to confine more efficiently the hot plasma, producing a flare evolution more similar to that described by 1D models.

It is worth emphasizing that our 3D simulation is focused on the effects of the flare on the stability of the disk and does not pretend to describe accurately the evolution of the flaring loop. Nevertheless, we show here that, even if the flare evolution is not described accurately, the length, maximum temperature, and peak X-ray luminosity of the flaring loop reproduced by our simulation resemble those derived from the analysis of the brightest X-ray flares observed in young low-mass stars (Favata et al. 2005). We are confident, therefore, that the flare simulated here is appropriate to investigate the effects of bright flares observed in young stars on the stability of the disk.

3.2 Dynamics of the accretion stream

During the flare evolution, the injected heat pulse produces an overpressure in the disk at the footpoint of the loop. This overpressure travels through the disk and reaches the opposite boundary after ≈ 5 hours, where it pushes the plasma out to form an intense funnel stream. Figure 5 shows the distributions of density and pressure in (R, z) slices passing through the middle of the stream. The overpressure wave triggering the stream is evident in the bottom panels. This new intense stream flows along the dipolar magnetic field lines and impacts onto the stellar surface ≈ 25 hours after the injection of the heat pulse. The right panels in Fig. 3 show a cutaway view of the star-disk system (upper panel) after the impact of the stream onto the stellar surface and a schematic view of the system during the stream evolution (lower panel). As a result, the stream accretes substantial mass onto the young star from the side of the disk opposite to the post-flare loop. Our 3D simulation follows the evolution of the accretion stream for additional 23 hours, for a total of 48 hours. In this time lapse the stream gradually approaches a quasi-stationary condition.

We analyzed the dynamics of the stream by deriving the forces at work along a fiducial magnetic field line nested within the stream. Initially the stream is triggered by a strong pressure gradient due to the overpressure wave originating from the flare. The pressure gradient force drives the material out of the disk and channels it into a funnel flow. Then the gravitational force accelerates the escaped material toward the central star. These forces evolve with time and Fig. 6 shows them along the fiducial field line after the stream impacts the stellar surface. At this stage, the pressure gradient is still effective in pushing the disk material out of the disk, but it acts in the opposite direction (against the free-fall of matter) in most of the accretion stream. The pressure gradient becomes the dominant force close to the stellar surface, substantially braking (but not stopping) the accretion flow. As discussed below, at this stage of evolution, the stream has not yet reached a quasi-stationary condition. Later, when the stream stabilizes, the gravitational force dominates the stream evolution and the plasma continuously accelerates toward the star, approaching the free-fall speed u_{ff} at the star’s photosphere. Other forces acting against the free-fall of matter are the centrifugal force and a backward force due to the magnetic mirror effect when the material approaches the star (see also Romanova et al. 2002; Zanni & Ferreira 2009). However, these forces are much smaller than the others and

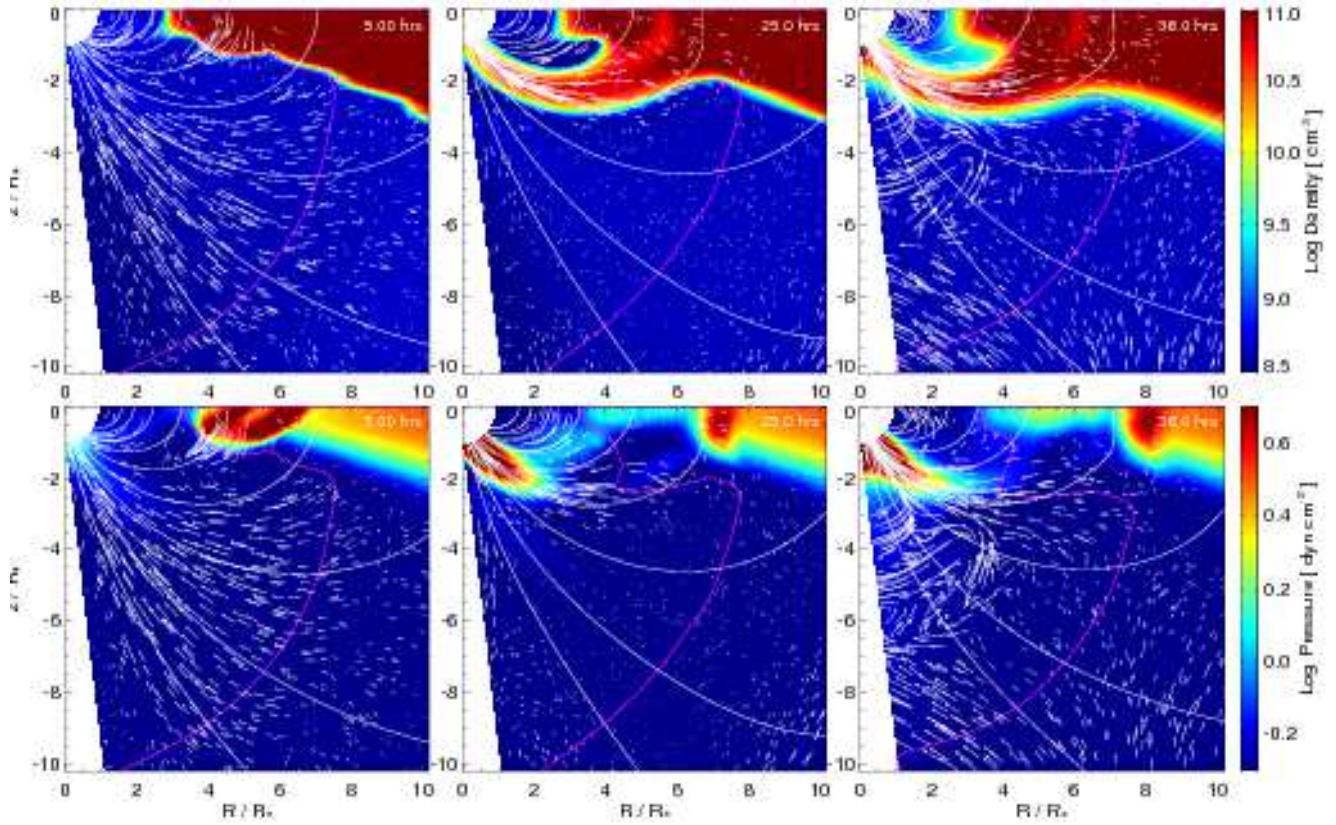


Figure 5. Close view of the accretion stream during its evolution. The figure shows slices in the (R, z) plane passing through the middle of the stream, reporting the distributions of density (upper panels) and pressure (lower panels). The slices encompass an angular sector going from the disk midplane to the rotation axis. The white lines represent sampled poloidal magnetic field lines. The arrows represent the poloidal flow velocities. The magenta line delimits the region with plasma $\beta < 1$ (on the left of each panel).

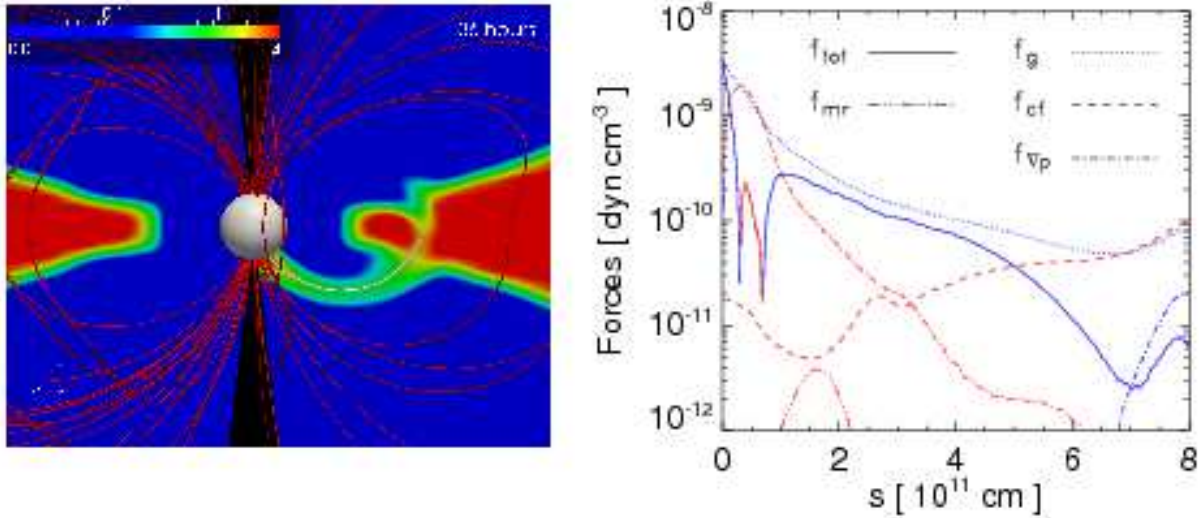


Figure 6. *Left panel:* two-dimensional section, in the (x, z) plane, of the particle number density distribution, in log scale, in units of 10^{11} cm^{-3} (see color table in the upper left corner of the panel) at the time $t = 36$ hours. The slice passes through the middle of the accretion stream. Selected magnetic field lines are overplotted in red; the white line represents a segment of a fiducial magnetic field line approximately in the middle of the accretion stream. *Right panel:* forces governing the stream dynamics versus the distance from the stellar surface along the fiducial field line in the left panel: f_{mr} is the backward force due to the magnetic mirror effect, f_{g} the gravitational force, f_{cf} the centrifugal force, $f_{\nabla p}$ the pressure gradient force, and f_{tot} the resultant force. Forces pushing the matter toward (away from) the star are in blue (red).

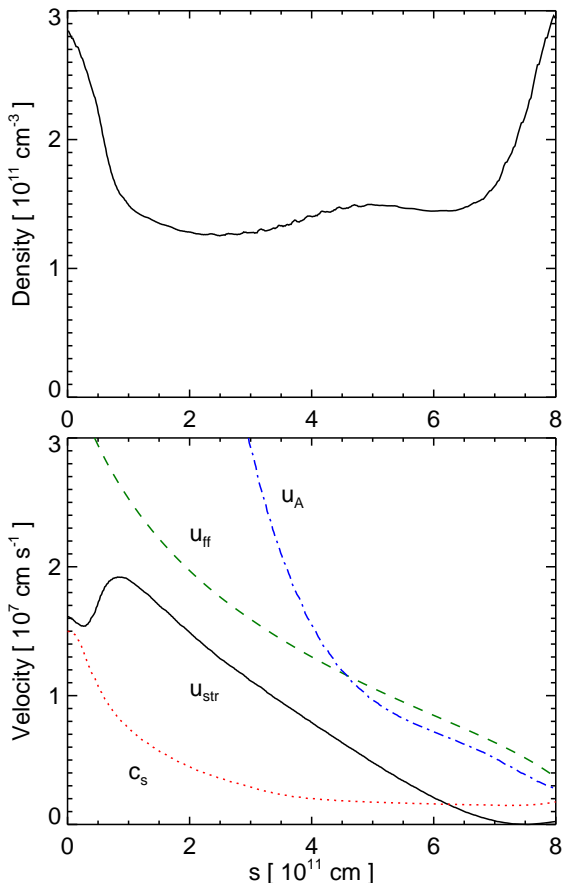


Figure 7. Profiles of particle number density (upper panel) and relevant velocities (lower panel) versus the distance s from the stellar surface along the fiducial magnetic field line shown in Fig. 6 at time $t = 36$ hours: u_{str} is the velocity of matter flowing along the accretion stream (solid black line), c_s the isothermal sound speed (dotted red line), u_{ff} the free-fall velocity (dashed green line), and u_A the Alfvén speed (dot-dashed blue line).

do not play any relevant role in the stream dynamics (Fig. 6; see also Romanova et al. 2002; Zanni & Ferreira 2009).

Figure 7 shows the profiles of particle number density and different velocities along the fiducial magnetic field line shown in Fig. 6 at time $t = 36$ hours. The matter flows with poloidal velocity u_{str} . The flow is accelerated by gravity and becomes supersonic at a distance of $\approx 2 \times 10^{11}$ cm from the disk, while the stream density decreases. The flow gradually approaches the free-fall velocity u_{ff} , reaching a maximum velocity of $u_{\text{str}} \approx 200 \text{ km s}^{-1}$ at $s \approx 10^{11}$ cm ($u_{\text{str}} \approx 0.8 u_{\text{ff}}$). Then the flow slightly brakes while the stream density increases again approaching the stellar surface. As discussed above, the slowdown of the flow is due to the pressure gradient force acting against the free-fall of matter for s ranging between 0.5×10^{11} and 1×10^{11} cm (see Fig. 6). This feature is present until the end of our 3D simulation at $t \approx 48$ hours.

To further investigate the evolution of the accretion stream, we performed an additional simulation with the same parameters of the 3D simulation discussed above but carried out in 2.5 dimensions (2.5D), that is, in spherical coordinates (R, θ) assuming axisymmetry around the rotation axis of the star-disk system. Note that, in this configuration,

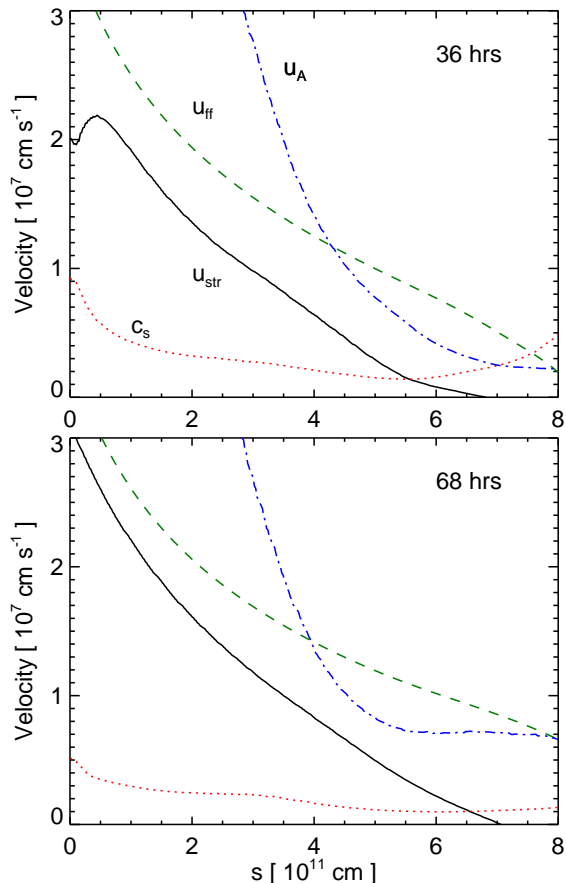


Figure 8. Profiles of velocity along the stream in the 2.5 D simulation. As in Fig. 7 for the profiles of relevant velocities with the distance s from the stellar surface along a fiducial magnetic field line nested within the stream at time $t = 36$ hours (upper panel) and $t = 68$ hours (lower panel).

the heat pulse is not localized in a relatively small portion of the disk (as in our 3D simulation), but is distributed in a ring. Nevertheless, we found that the evolution of the flare and the stream described by the 2.5D simulation is quite similar to that of our 3D simulation. The 2.5D simulation allowed us to extend our analysis of the stream dynamics, following its evolution until $t = 100$ hours (i.e. approximately four days). Figure 8 shows the profiles of the relevant velocities derived from the 2.5D simulation at $t = 36$ hours (upper panel) and $t = 68$ hours (lower panel). The velocity profiles at $t = 36$ hours resemble those derived from the 3D simulation (lower panel in Fig. 7). In particular, the flow slightly brakes approaching the stellar surface due to a pressure gradient force slowing down the free-fall of matter, as found in the 3D simulation. In addition, the 2.5D simulation shows that, at this stage, the stream has not reached yet a quasi-stationary condition. Later, the stream stabilizes (after $t \approx 60$ hours); the gravitational force becomes dominant along the stream and the matter is accelerated until it impacts the stellar surface, reaching there a maximum velocity of $u_{\text{str}} \approx 300 \text{ km s}^{-1}$ corresponding to $\approx 0.9 u_{\text{ff}}$.

The above results, therefore, show that the physical characteristics of the accretion stream triggered by the flare closely recall those, largely discussed in the literature, of

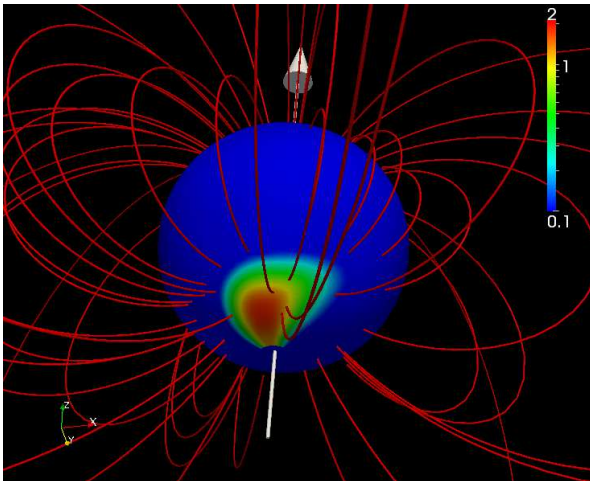


Figure 9. Particle number density distribution on the stellar surface, in log scale, in units of 10^{11} cm^{-3} (see color table on the right of the panel) at the time $t = 36$ hours. Selected magnetic field lines are overlotted in red. The white arrow marks the rotation axis of the star.

streams driven by the accumulation of mass at the disk truncation radius under the effect of the viscosity and pushed out of the equatorial plane because of the growing pressure gradient there (Romanova et al. 2002, 2003; Bessolaz et al. 2008; Zanni & Ferreira 2009). Our simulation shows that the stream is relatively cold (its temperature remains below 1 MK). After the disk material enters the stream, its density slightly decreases and, close to the stellar surface, increases again as a result of the gas compression by the dipolar magnetic field. The stream velocity u_{str} gradually increases toward the star: it becomes supersonic already at a distance of $\approx 2 \times 10^{11}$ cm from the disk, and u_{str} approaches the free-fall speed u_{ff} close to the stellar surface. Figure 9 shows the density distribution on the stellar surface at $t = 36$ hours; the dense spot on the surface is the region of impact of the stream. The spot covers a small percentage of the stellar surface and the stream is inhomogeneous with its mass density varying across the stream and being the largest in the inner region, according to Romanova et al. (2004).

Finally, we derived the mass accretion rate \dot{M} due to the stream from the side of the disk opposite to the post-flare loop and found $\dot{M} \gtrsim 2.5 \times 10^{-10} M_{\odot} \text{ yr}^{-1}$. Accretion rates derived from optical-near UV continuum emission typically range between 10^{-12} and $10^{-6} M_{\odot} \text{ yr}^{-1}$ with \dot{M} varying in the same star even by a factor of 10 and depending on the age and mass of the star (Muzerolle et al. 2005; Mohanty et al. 2005; Natta et al. 2006). In general, more evolved low-mass young stars are characterized by lower accretion rates (e.g. Herczeg & Hillenbrand 2008 and references therein). We compared the rate \dot{M} derived from our 3D simulation with the rates derived from optical-UV observations and available in the literature. In particular, we considered a sample of low-mass stars and brown dwarfs observed with LRIS on Keck I and a sample of solar-mass young accretors observed with HST STIS (both samples analyzed by Herczeg & Hillenbrand 2008), and an X-ray selected sample of CTTSs observed with various optical telescopes (analyzed by Curran et al. 2011). Herczeg & Hillenbrand (2008) found that the excess UV and optical emission arising in the

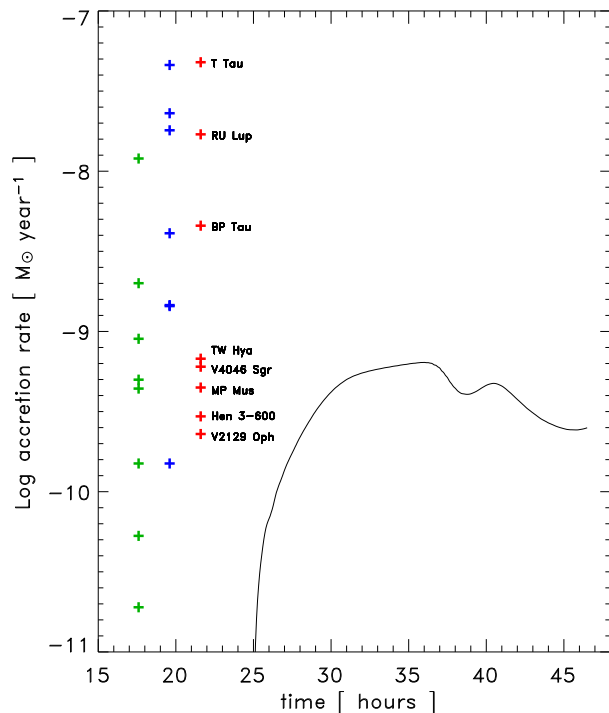


Figure 10. The solid line shows the mass accretion rate during the evolution of the funnel flow developed on the side of the disk opposite to the flaring loop. The crosses report the values of mass accretion rate derived from optical-near UV observations for a sample of low-mass stars and brown dwarfs (green; Herczeg & Hillenbrand 2008), for a sample of solar-mass young accretors (blue; Herczeg & Hillenbrand 2008) and for an X-ray-selected sample of CTTSs (red; Curran et al. 2011).

Balmer and Paschen continua yields mass accretion rates ranging between 2×10^{-12} and $10^{-8} M_{\odot} \text{ yr}^{-1}$ in the case of low-mass stars and brown dwarfs, and ranging between 2×10^{-10} and $5 \times 10^{-8} M_{\odot} \text{ yr}^{-1}$ in the case of solar-mass stars. Curran et al. (2011) calculated \dot{M} for the stars of their sample by measuring $H\alpha$, $H\beta$, $H\gamma$, He II (4686 Å), He I (5016 Å), He I (5876 Å) O I (6300 Å), and He I (6678 Å) equivalent widths and found that the mass accretion rates range between 2×10^{-10} and $5 \times 10^{-8} M_{\odot} \text{ yr}^{-1}$. Figure 10 shows the rate \dot{M} derived from our 3D simulation compared with the three samples of young accreting stars. The accretion rate of our simulation is in the range of the rates measured in low-mass stars and lower than those of fast-accreting objects as BP Tau, RU Lup, or T Tau.

4 SUMMARY AND CONCLUSIONS

We investigated the evolution of a bright flare occurring close to the disk surrounding a magnetized CTTS and its effects on the stability of the disk, through numerical MHD simulations. To our knowledge, the simulation presented here represent the first attempt to model the 3D global evolution of the star-disk system that simultaneously include stellar gravity, viscosity of the disk, magnetic field, radiative cooling, and magnetic-field-oriented thermal conduction (including the effects of heat flux saturation). Our findings lead to several conclusions:

(i) During its first stage of evolution, the flare gives rise to a hot magnetic loop linking the inner part of the disk to the star; we found that the length, maximum temperature, and peak X-ray luminosity of the simulated flaring loop are similar to those derived from the analysis of luminous X-ray flares observed in young low-mass stars (Favata et al. 2005).

(ii) During the flare evolution, disk material evaporates in the outer stellar atmosphere under the effect of the thermal conduction. A small fraction of the evaporated disk material gradually fills the loop in ≈ 10 hours. Indeed most part of the evaporated disk material is not efficiently confined by the magnetic field and channeled into the loop but is rather ejected away from the central star in the outer stellar corona, carrying away mass and angular momentum.

(iii) In the aftermath of the flare, the disk is strongly perturbed: the injected heat pulse produces an overpressure in the disk at the loop’s footpoint that travels through the disk. When the overpressure reaches the opposite side of the disk, a funnel flow starts to develop there, flowing along the dipolar magnetic field lines and impacting onto the stellar surface ≈ 1 day after the injection of the heat pulse.

(iv) We found that the mass accretion rate \dot{M} of the stream triggered by the flare is in good agreement with those measured in low-mass stars and brown dwarfs and in some solar-mass accretors (e.g. Herczeg & Hillenbrand 2008; Curran et al. 2011). The stream therefore accretes substantial mass (comparable with those observed) onto the young star from the side of the disk opposite to the post-flare loop.

We conclude therefore that the brightest flares detected in CTTSs (e.g. Favata et al. 2005) can be a mechanism to trigger mass accretion episodes onto protostars with accretion rates in the range of those measured in low-mass stars and lower than those of fast-accreting objects. On the other hand, it is worth mentioning that large flares do not occur continuously in CTTSs and therefore cannot explain alone the time-averaged accretion rates derived in young accretors: an average of 1 flare per star per 650 ks (≈ 7 days) has been inferred by analyzing the COUP observations (Wolk et al. 2005) and clusters much older than Orion (Wolk et al. 2004). To ascertain the contribution that flares may have to the observed time-averaged accretion rates, it is necessary to determine the frequency of those flares able to trigger accretion streams. In the future, an exploration of the parameter space of our model is therefore needed to determine to which extent the total energy released during the flare can be reduced to still produce an accretion stream. This point is rather important to ascertain if a storm of small-to-medium flares (very frequent in CTTSs and often not even resolved in the lightcurves) occurring on the accretion disk of young stars is able to trigger accretion streams with high cadence, thus leading to a significant and persistent mass accretion. This issue deserves further investigation in future studies.

The initial conditions adopted in our simulations are largely used in the literature (e.g. Romanova et al. 2002 and subsequent works) and are appropriate to describe the star-disk system in CTTSs. However, as discussed in Sect. 3.1, these conditions may result to be idealized and simplified in some aspects. Many observations indicate that the stellar atmospheres are permeated by magnetic fields with a degree of complexity much higher than the magnetic dipole adopted here (e.g. Gregory et al. 2010 and references therein); the

flare may occur in the presence of existing accretion streams induced by the coupling of the magnetic field to the disk below the corotation radius (e.g. Romanova et al. 2002, 2003; Bessolaz et al. 2008; Zanni & Ferreira 2009) or triggered by other flares. In particular, the magnetic field in proximity of the heat release (due to magnetic reconnection) is expected to be more complex than that modeled here, thus confining more efficiently the hot plasma and enhancing the effects of the flare energy deposition on the system. On the other hand, the flaring loop and the flare-induced accretion stream could be strongly modified or even disappear if the flare occurs in a flux tube initially filled with cold infalling gas. However, Reale (2009) showed that a flare involving dense infalling plasma would decay much faster than generally observed, so that the flares we address here do not occur in such a configuration. Nevertheless, the flaring loop and the flare-induced accretion stream may be strongly perturbed and have a more complex structure than that described here if the flare energy release occurs in proximity of an existing accretion stream.

Following other works in the literature (e.g. Romanova et al. 2002, 2003, 2004; Kulkarni & Romanova 2008), we assumed the turbulent diffusivity to be uniform within the disk, setting α as a constant. However numerical simulations indicate that the MRI stress would be substantial in the disk midplane where the plasma β is high, but would drop in outer disk layers where β is relatively low. As a result, the turbulent diffusivity, scaled appropriately to the MRI, is expected to be smaller in the outer disk layers than in the disk midplane. Since the α value adopted in our simulation (namely $\alpha = 0.02$) lies in the lower limit of the range of the parameter α (namely $0.01 \leq \alpha \leq 0.6$; Balbus 2003; Kulkarni & Romanova 2008), we expect that the turbulent diffusivity would be larger in the disk midplane than assumed in our simulation, thus influencing the mass accretion from the disk onto the star. However, the time lapse covered by our simulation (≈ 48 hours) is $\approx 1/5$ of the star rotation period which is much shorter than the time required by the turbulent diffusivity (namely several star rotation periods; Romanova et al. 2002, 2003; Bessolaz et al. 2008; Zanni & Ferreira 2009) to be effective and trigger magnetospheric funnel streams. In fact, throughout the simulation, no stream develops in disk regions not influenced by the flare although our model includes the disk viscosity.

As an additional check, we performed 2.5D simulations with the same parameters of the 3D simulation but exploring the effect of α in the range between 0.02 and 0.1, and considering simulations either with or without the disk viscosity. We found that the viscosity does not significantly influence the results over the time laps covered by the 3D simulation. We conclude therefore that a bright flare occurring close to the circumstellar disk can trigger a substantial and long-lasting accretion flow with physical characteristics similar to those caused by the disk viscosity². This new mechanism to drive mass accretion might be general. We suggest that the flaring activity common to CTTSs may turn out to be an

² Note that, as discussed above, Reale (2009) has shown that the opposite is unlikely, that is flares cannot be triggered in an accreting flux tube.

important factor in the exchange of angular momentum and mass between the circumstellar disk and the central protostar. This exchange is a rather hot and controversial topic in astrophysics and our research contributes to this issue, by exploring the role of the bright flares detected in CTTSS (Favata et al. 2005) not considered up to now.

Our model predicts that the stream triggered by a flare impacts the stellar surface with a delay of ≈ 1 day since the peak X-ray luminosity of the flare. This time delay depends on the physical parameters of the model, namely the disk truncation radius, the mass density and thickness of the disk, and the energy released by the heat pulse. We expect therefore that the accretion shock generated by the impact of the stream on the stellar surface might be visible with a delay of the order of few days after the X-ray flare. Unfortunately, even if this is the case, revealing both the X-ray flare and the delayed accretion shock in real systems would be a rather difficult task because: 1) the star needs to be almost edge-on to allow both the flaring loop and the accretion shock (located in different hemispheres of the star) to be observable; 2) both the flaring loop and the accretion shock should not be eclipsed by the star (or strongly absorbed by the circumstellar material) during the observation. A more feasible task could be to detect the effects of the X-ray irradiation of the disk by the flare located just above it. For instance, a photoevaporation of disk material by the X-ray emission from the flare is expected to be almost instantaneous with the flare at variance with the case of a flare occurring on the star which is assumed to be delayed given the distance of the inner edge of the disk from the star. Searching for a tight correlation between X-ray flares and variability in IR or optical band associated with the photoevaporation of the disk could be an indication that the flares were located close to the disk.

In addition to the results presented above, our simulation opens a number of interesting issues. We have shown that the flaring loop linking the disk with the star is a bright X-ray source, irradiating the disk from above, at variance with the stellar corona which irradiates only the innermost part of the disk. We suggest that this kind of sources may strongly influence the chemical and physical evolution of the disk, reaching parts of it that are effectively shielded from the stellar coronal X-ray emission, with important consequences, for instance, on the formation of planets. The turbulence and ionization state of plasma resulting from the irradiance of the disk by the flaring loop may also interact (because of the change of ionization and electrical conductivity) in a nontrivial way with the MRI. Thus it is reasonable to suspect that the effects of this X-ray radiation may influence the efficiency of MRI and, therefore, the efficiency of angular momentum transport within the disk. All these issues deserve further investigations.

ACKNOWLEDGMENTS

We thank an anonymous referee for constructive and helpful criticism. We acknowledge stimulating discussions with C. Argiroffi, E. Flaccomio, J. Kastner, A. Maggio, G. Micela, T. Montmerle, and S. Sciortino. PLUTO is developed at the Turin Astronomical Observatory in collaboration with the Department of General Physics of the Turin University.

All computations were performed on the IBM/Sp6 supercomputer at CINECA (Bologna, Italy), and at the HPC facility (SCAN) of the INAF - Osservatorio Astronomico di Palermo. This work was supported by the EU Marie Curie Transfer of Knowledge program PHOENIX under contract No. MTKD-CT-2005-029768.

REFERENCES

- Aarnio A. N., Stassun K. G., Matt S. P., 2010, *Astrophys. J.*, 717, 93
- Alexiades V., Amiez G., Gremaud P. A., 1996, *Communications in Numerical Methods in Engineering*, 12, 31
- Anders E., Grevesse N., 1989, *Geochim. Cosmochim. Acta*, 53, 197
- Armitage P. J., 1998, *Astrophys. J.*, 501, L189
- Audard M., Briggs K. R., Grosso N., Güdel M., Scelsi L., Bouvier J., Telleschi A., 2007, *Astron. & Astrophys.*, 468, 379
- Balbus S. A., 2003, *Ann. Rev. Astron. Astrophys.*, 41, 555
- Balbus S. A., Hawley J. F., 1991, *Astrophys. J.*, 376, 214
- Balbus S. A., Hawley J. F., 1998, *Reviews of Modern Physics*, 70, 1
- Balsara D. S., Spicer D. S., 1999, *Journal of Computational Physics*, 149, 270
- Bessolaz N., Zanni C., Ferreira J., Keppens R., Bouvier J., 2008, *Astron. & Astrophys.*, 478, 155
- Bisnovaty-Kogan G. S., Lovelace R. V. E., 2001, *New A Rev.*, 45, 663
- Bodo G., Mignone A., Cattaneo F., Rossi P., Ferrari A., 2008, *Astron. & Astrophys.*, 487, 1
- Borkowski K. J., Shull J. M., McKee C. F., 1989, *Astrophys. J.*, 336, 979
- Bouvier J., Appenzeller I., eds, 2007, *Star-Disk Interaction in Young Stars Vol. 243 of IAU Symposium*
- Brandenburg A., Nordlund A., Stein R. F., Torkelsson U., 1995, *Astrophys. J.*, 446, 741
- Brown J. C., Spicer D. S., Melrose D. B., 1979, *Astrophys. J.*, 228, 592
- Cowie L. L., McKee C. F., 1977, *Astrophys. J.*, 211, 135
- Curran R. L., Argiroffi C., Sacco G. G., Orlando S., Peres G., Reale F., Maggio A., 2011, *Astron. & Astrophys.*, 526, A104
- Fadeyev Y. A., Le Coroller H., Gillet D., 2002, *Astron. & Astrophys.*, 392, 735
- Favata F., Flaccomio E., Reale F., Micela G., Sciortino S., Shang H., Stassun K. G., Feigelson E. D., 2005, *Astrophys. J. Suppl.*, 160, 469
- Feigelson E. D., Montmerle T., 1999, *Ann. Rev. Astron. Astrophys.*, 37, 363
- Fromang S., Papaloizou J., 2007, *Astron. & Astrophys.*, 476, 1113
- Getman K. V., Feigelson E. D., Grosso N., McCaughrean M. J., Micela G., Broos P., Garmire G., Townsley L., 2005, *Astrophys. J. Suppl.*, 160, 353
- Giuliani J. L., 1984, *Astrophys. J.*, 277, 605
- Gregory S. G., Jardine M., Gray C. G., Donati J., 2010, *Reports on Progress in Physics*, 73, 126901 (28pp)
- Hartmann L., 1998, *Accretion Processes in Star Formation*. New York: Cambridge University Press; Cambridge astrophysics series; 32

- Hawley J. F., 2000, *Astrophys. J.*, 528, 462
- Hawley J. F., Gammie C. F., Balbus S. A., 1995, *Astrophys. J.*, 440, 742
- Hayashi M. R., Shibata K., Matsumoto R., 1996, *Astrophys. J.*, 468, L37
- Herczeg G. J., Hillenbrand L. A., 2008, *Astrophys. J.*, 681, 594
- Hirose S., Krolik J. H., Stone J. M., 2006, *Astrophys. J.*, 640, 901
- Hujeirat A., 2005, *Computer Physics Communications*, 168, 1
- Hujeirat A., Camenzind M., 2000, *Astron. & Astrophys.*, 362, L41
- Johns-Krull C. M., Valenti J. A., Hatzes A. P., Kanaan A., 1999, *Astrophys. J.*, 510, L41
- Kashyap V., Drake J. J., 2000, *Bulletin of the Astronomical Society of India*, 28, 475
- King A. R., Pringle J. E., Livio M., 2007, *Mon. Not. R. Astron. Soc.*, 376, 1740
- Koenigl A., 1991, *Astrophys. J.*, 370, L39
- Kulkarni A. K., Romanova M. M., 2008, *Mon. Not. R. Astron. Soc.*, 386, 673
- Mignone A., Bodo G., Massaglia S., Matsakos T., Tesileanu O., Zanni C., Ferrari A., 2007, *Astrophys. J. Suppl.*, 170, 228
- Mohanty S., Jayawardhana R., Basri G., 2005, *Astrophys. J.*, 626, 498
- Muzerolle J., Luhman K. L., Briceño C., Hartmann L., Calvet N., 2005, *Astrophys. J.*, 625, 906
- Natta A., Testi L., Randich S., 2006, *Astron. & Astrophys.*, 452, 245
- Orlando S., Bocchino F., Peres G., Reale F., Plewa T., Rosner R., 2006, *Astron. & Astrophys.*, 457, 545
- Orlando S., Bocchino F., Reale F., Peres G., Pagano P., 2008, *Astrophys. J.*, 678, 274
- Orlando S., Drake J. J., Laming J. M., 2009, *Astron. & Astrophys.*, 493, 1049
- Orlando S., Peres G., Reale F., Bocchino F., Rosner R., Plewa T., Siegel A., 2005, *Astron. & Astrophys.*, 444, 505
- Orlando S., Sacco G. G., Argiroffi C., Reale F., Peres G., Maggio A., 2010, *Astron. & Astrophys.*, 510, A71
- Powell K. G., Roe P. L., Linde T. J., Gombosi T. I., de Zeeuw D. L., 1999, *Journal of Computational Physics*, 154, 284
- Reale F., 2009, in K. Tsinganos, T. Ray, & M. Stute ed., *Protostellar Jets in Context Flaring Activity in Accretion Flows of Young Stellar Objects*. pp 179–183
- Reale F., Bocchino F., Peres G., 2002, *Astron. & Astrophys.*, 383, 952
- Reale F., Orlando S., 2008, *Astrophys. J.*, 684, 715
- Reale F., Peres G., Serio S., Rosner R., Schmitt J. H. M. M., 1988, *Astrophys. J.*, 328, 256
- Romanova M. M., Ustyugova G. V., Koldoba A. V., Lovelace R. V. E., 2002, *Astrophys. J.*, 578, 420
- Romanova M. M., Ustyugova G. V., Koldoba A. V., Lovelace R. V. E., 2004, *Astrophys. J.*, 610, 920
- Romanova M. M., Ustyugova G. V., Koldoba A. V., Wick J. V., Lovelace R. V. E., 2003, *Astrophys. J.*, 595, 1009
- Shakura N. I., Sunyaev R. A., 1973, *Astron. & Astrophys.*, 24, 337
- Shu F. H., Shang H., Glassgold A. E., Lee T., 1997, *Science*, 277, 1475
- Smith R. K., Brickhouse N. S., Liedahl D. A., Raymond J. C., 2001, *Astrophys. J.*, 556, L91
- Spitzer L., 1962, *Physics of Fully Ionized Gases*. New York: Interscience, 1962
- Tanaka T., 1994, *Journal of Computational Physics*, 111, 381
- Telleschi A., Güdel M., Briggs K. R., Audard M., Scelsi L., 2007, *Astron. & Astrophys.*, 468, 443
- Wolk S. J., Harnden Jr. F. R., Flaccomio E., Micela G., Favata F., Shang H., Feigelson E. D., 2005, *Astrophys. J. Suppl.*, 160, 423
- Wolk S. J., Harnden Jr. F. R., Murray S. S., Adams N. R., Damiani F., Flaccomio E., Micela G., Sciortino S., Jeffries R. D., 2004, *Astrophys. J.*, 606, 466
- Zanni C., Ferreira J., 2009, *Astron. & Astrophys.*, 508, 1117